Geophys. J. Int. (1996) **127**, 708–718

Free-surface formulation of mantle convection—I. Basic theory and application to plumes

Shijie Zhong, Michael Gurnis and Louis Moresi*
Seismological Laboratory, California Institute of Technology, Pasadena, CA 91125, USA

Accepted 1996 August 9. Received 1996 August 5; in original form 1995 November 22

SUMMARY

In mantle convection models, the top surface is traditionally approximated as a free-slip boundary, and the dynamic topography is obtained by assuming that the normal stress on the free-slip boundary is compensated instantaneously through surface deformation. It has already been shown that this approximation is valid for long-wavelength topography. Based on both viscous and viscoelastic models with a free surface, we have found that the characteristic time for topographic growth is comparable to the timescales of mantle convection ($\sim 10^6$ year) for short and intermediate wavelengths (10^3 km or less) and/or a high effective lithospheric viscosity ($> 10^{24}$ Pa s). This suggests that the topography is history-dependent under these conditions and that a free-surface formulation is required to study the topography at these wavelengths.

We have developed a new Eulerian finite-element technique to model a free surface. Since the technique is based upon an undeformable Eulerian grid, this enables us to study long-term, free-surface dynamics in the presence of evolving buoyancy. We have compared numerical with analytic solutions of viscous relaxation for fixed buoyancy problems. As long as the magnitude of topography is much smaller than the wavelength, we find that the finite-element method is very accurate, with relative errors of less than 1 per cent. This numerical technique can be applied to a variety of geophysical problems with free surfaces. In applying this technique to dynamic models of mantle plumes, we find that surface relaxation retards the topography at intermediate and short wavelengths and produces a smoother topography, compared with topography from free-slip calculations. This reduced topography has a significant influence on the geoid at the corresponding wavelengths. Moreover, free-surface models, by allowing vertical motion on the free surface, yield a hotter lithosphere over ascending plumes than models with free-slip boundaries.

Key words: geoid, mantle convection, plume, rheology, topography.

INTRODUCTION

The Earth's surface is stress-free and dynamically responds to variations in surface and subcrustal loads. The Earth's mantle is viscoelastic. Because of the temperature dependence of silicate rheology, there is an extremely high viscosity near the Earth's surface and a relatively small viscosity at depth; the shallow part of the lithosphere may deform approximately in an elastic fashion while the deep mantle interior deforms viscously in response to long-term loads. The surface deformation associated with postglacial rebound in Fennoscandia and North America is well documented (Haskell 1935; Cathles 1975). The observed relaxation time for postglacial rebound is about 10^4 years. Models with a purely elastic lithosphere overlying a viscous mantle yield a 100 km thick elastic lithosphere and 10^{21} Pa s mantle viscosity (e.g. McConnell 1968; Cathles 1975). Independently, the apparent elastic thickness of oceanic lithosphere can be constrained by matching sea-floor topography near oceanic trenches and seamounts with the deflection of a thin elastic plate (Watts, Bodine & Ribe 1980). The elastic thickness of oceanic lithosphere ranges from a few kilometres in young lithosphere to tens of kilometres in old ocean basins (Watts *et al.* 1980).

Mantle buoyancy, such as that caused by cold and dense subducted slabs, results in dynamic topography that has an important influence on the geoid (Hager 1984; Ricard, Fleitout & Froidevaux 1984). Studies of topography induced by mantle convection assume that the mantle and lithosphere deform simply by viscous flow in a quasi-steady state. This assumption,

* Now at: Research School of Earth Sciences, Australian National University, Canberra, ACT 0200, Australia.

in general, is justified because the timescale for mantle convection ($>10^6$ years) is much larger than the Maxwell time of the mantle (about 10^3 years) and because inertial forces in mantle convection are negligible. In these viscous-flow models, it has been assumed that boundaries are free-slip (i.e. *boundaries with zero normal velocity and zero shear stress*), and that the normal stress generated by internal buoyancy on free-slip boundaries is instantaneously compensated by dynamic topography. The characteristic time for developing dynamic topography (i.e. viscous relaxation time) is generally small compared with the timescale of mantle convection. Since the shallow part of the lithosphere deforms in an approximately elastic manner, the effective viscosity of the lithosphere is significant in determining the viscous relaxation time in purely viscous-flow models. Richards & Hager (1984) showed that the viscous relaxation time is about 10^4 years for topography with a wavelength greater than 2×10^3 km (or spherical harmonic degree 20) and a lithosphere with an effective viscosity 100 times larger than the mantle viscosity (about 10^{21} Pa s). However, this relaxation time increases with a higher-viscosity and a shorter-wavelength topography (Cathles 1977). With a viscoelastic model of subducted slabs, Gurnis, Eloy & Zhong (1996; Part II) have shown that the relaxation time for back-arc basin topography can be as large as 10^6 years for reasonable viscosity structures. If the relaxation time for a particular wavelength is comparable to mantle convection timescales, then the relaxation of topography needs to be considered in determining the topography, i.e. the topography is history-dependent. In this limit, we cannot determine the topography from normal stress acting on free-slip boundaries based on the quasi-steady-state assumption; instead we may be required to represent boundaries as natural free surfaces (i.e. *boundaries with zero shear and normal stresses*) which dynamically evolve with time.

The effective viscosity of lithosphere is not well constrained. Dynamic models of mantle convection suggest that the effective viscosity of lithosphere is significantly higher than the upper-mantle viscosity in order to give rise to a 'plate-like' surface velocity (King, Raefsky & Hager 1990) and to stabilize the top thermal boundary layer (Davies 1988). However, these arguments do not provide an upper bound on the effective lithospheric viscosity. It has been proposed that the base of the elastic plate is defined by the 650 °C isotherm (Watts *et al.* 1980; Anderson 1995). Since the base of the lithosphere (including both elastic and high-viscosity lithosphere) has a temperature of about 1200 °C, the 650 °C temperature drop from the base of the lithosphere to the base of the elastic plate would give seven orders of magnitude viscosity increase if a dry olivine rheology is assumed (Karato & Wu 1993). Although other factors, including stress dependence, may complicate the rheology, it is likely that the effective viscosity of lithosphere is higher than the 10^{23} Pa s used by Richards & Hager (1984). On the other hand, studies on intermediate- and short-wavelength (10^3 km or less) topography and/or geoid with regional models of subducted slabs, spreading centres, and mantle plumes are of fundamental importance (e.g. Richards, Hager & Sleep 1988; Chen & Morgan 1990; Zhong & Gurnis 1994). It is important to examine the conditions under which the relaxation has an important influence on the topography and geoid.

For internally loaded problems, we have studied the influence of relaxation on topography and geoid as a function of wavelength and viscosity structure. Based on both viscoelastic and purely viscous-flow models, we have found that the relaxation time for intermediate- and short- (1000 km or less) wavelength topography is strongly dependent on the effective viscosity of the lithosphere and is close to 10^6 yr if the effective viscosity of the lithosphere is 10^{24} Pa s or larger. For a wavelength longer than 2000 km, the relaxation time from purely viscous-flow models can still be more than 10^6 yr for very large lithosphere viscosities; however, the relaxation time from the more realistic viscoelastic models is always less than 10^4 yr, independent of the effective viscosity of lithosphere. The effects of surface relaxation are further examined by comparing free-surface with free-slip models of topography over ascending mantle plumes. The surface relaxation tends to reduce the magnitude of topography and to smooth the topography over plumes. This has a significant influence on the geoid. Moreover, the vertical motion on the free surface also influences the temperature in the shallow part of the mantle.

In what follows, we first present our models and governing equations. Second, we introduce a simple technique to incorporate free surfaces into Eulerian finite-element models of mantle convection and prove the validity of this technique by comparing numerical with analytic solutions. Third, we show the relaxation times from viscoelastic and purely viscous-flow models for various wavelengths and viscosity structures. Fourth, time-dependent convection models of ascending mantle plumes are used to show the influence of surface relaxation on the topography and geoid. Finally, we discuss the geophysical implications of our results.

GOVERNING EQUATIONS AND NUMERICAL METHODS

The momentum, continuity and energy equations for the mantle are, respectively,

$$\sigma_{ij,j}+f_i=0, \tag{1}$$

$$u_{i,i}=0, \tag{2}$$

$$\frac{\partial T}{\partial t}+u_i\cdot T_{,i}=\kappa T_{,ii}+H, \tag{3}$$

where u_i, f_i, and σ_{ij} are the flow velocity, the body force, and the stress tensor, respectively; i and j are spatial indices; T is the temperature; t is the time; κ is the thermal diffusivity; and H is the heat source. The body force can be related to temperature T as

$$(f_1, f_2)=(0, -\rho_0[1-\alpha(T-T_0)]g). \tag{4}$$

The constitutive equations for viscous and viscoelastic (Maxwell body) media are, respectively,

$$\dot{e}_{ij}=\frac{1}{2\mu}(\sigma_{ij}+P\delta_{ij}), \tag{5}$$

$$\dot{e}_{ij}=\frac{1+\nu}{E}\dot{\sigma}_{ij}-\frac{\nu}{E}\dot{\sigma}_{kk}\delta_{ij}+\frac{1}{2\mu}\left(\sigma_{ij}-\frac{1}{3}\sigma_{kk}\delta_{ij}\right). \tag{6}$$

In (4), (5), and (6), ρ_0 and T_0 refer to the reference density and temperature, respectively; g is the gravitational acceleration; α is the coefficient of thermal expansion; P is the pressure; and μ is the dynamic viscosity; $\dot{e}_{ij}$ is the strain rate given by $\dot{e}_{ij}=(u_{i,j}+u_{j,i})/2$; E is Young's modulus; and ν is Poisson's ratio.

Our models are in 2-D Cartesian geometry. The initial and boundary conditions will be discussed below when necessary. Both viscous and viscoelastic models are computed. For viscous models, we use the finite-element code ConMan (King *et al.* 1990) to solve the governing equations (1)–(3). For viscoelastic models, we use the finite-element code TECTON (Melosh & Raefsky 1980) to solve the momentum equation. The viscoelastic models are only used to compute relaxation times of surface loads like postglacial rebound problems, while the viscous-flow models are used for studying surface relaxation with internal loads. The viscous-flow models are also used for studying the long-term evolution of surface topography over ascending plumes. Model parameters are listed in Table 1.

In order to study the relaxation of topography, it is necessary to incorporate free surfaces into time-dependent convection models. A conventional approach for tracking a free-surface is to use a Lagrangian formulation in which the grid deforms. This technique is used in the code TECTON for viscoelastic problems (Melosh & Raefsky 1980). However, the Lagrangian formulation cannot be effectively applied to mantle convection problems which involve large deformation on a large temporal scale, unless an efficient remeshing scheme is used (e.g. Poliakov & Podladchikov 1992). Recently, Braun & Sambridge (1995) introduced a new Lagrangian technique which may relieve this situation somewhat. We find that we can use a Eulerian formulation to study the evolution of free surfaces as long as the magnitude of the surface vertical deformation is much smaller than the wavelength of the deformed free surface.

In our approach, we treat a free surface as a pseudo free surface whose coordinates are fixed on a Eulerian grid. We update the topography of our free surface by using the vertical velocity on the pseudo free surface and then apply the resulting topography as boundary-normal stress on the top of the Eulerian grid when updating the velocity (Fig. 1). Since the grid does not vary with time, this approach can be used to study free surfaces with large and complex internal deformations of the kind that arise in thermal convection over a long time. By making a comparison with analytic solutions of surface relaxation problems, we find that this approach is very accurate, as long as a time increment is substantially smaller than a characteristic time for evolution of a free surface. This method is very similar to the arbitrary Lagrangian–Eulerian (ALE) algorithm (e.g. Hughes, Liu & Zimmermann 1981). In the ALE algorithm in two dimensions, x and z velocity components can each be described in either a Lagrangian or a Eulerian frame, and the mesh only deforms for velocity components in the Lagrangian frame (Hughes *et al.* 1981). In our method, we can view vertical velocities on free surfaces as in a Lagrangian frame and all other velocities as in the Eulerian frame. Since the ratio of amplitude to wavelength of topography on our free surfaces is small, the vertical deformation in each element bounded by the free surfaces is sufficiently uniform that we can treat the deformed element simply as a stretched element. Therefore, we can apply the resulting normal stress on the original elements to account for

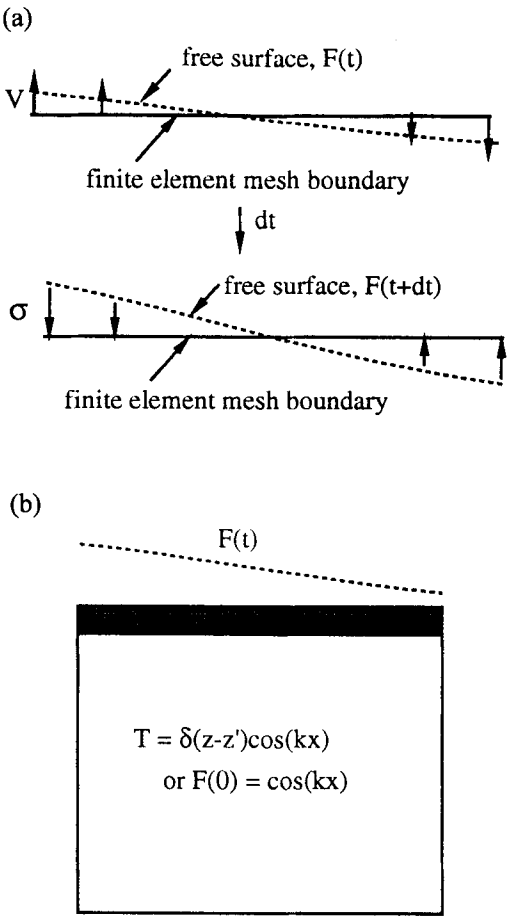

Figure 1. (a) Illustration of the pseudo-free-surface algorithm. (b) Models with free surfaces for studying the surface relaxation for different viscosity structures and driving forces.

Table 1. Physical and geometrical model parameters.

Thickness of the fluid layer, D	3×10^6 m
Boundary of the upper and lower mantle	6.7×10^5 m
Temperature contrast, $T_b - T_o$	2000 K
Reference density, ρ_o	3.3×10^3 kg m^{-3}
Thermal diffusivity, κ	10^{-6} m^2 s^{-1}
Acceleration of gravity, g	10 m s^{-2}
Thermal expansion, α	2.0×10^{-5} K^{-1}
Young's Modulus*	1.75×10^{11} Pa
Poisson's ratio*	0.499999

* only used in viscoelastic models.

the effect of the deformed mesh without actually deforming the element bounded by the free surfaces.

RESULTS

In this section, we will first verify the validity of our pseudo-free-surface algorithm. Second, we will determine the surface relaxation time from viscoelastic and purely viscous-flow models as a function of wavelength and viscosity structure. Finally, we will isolate the influence of surface relaxation on topography and its commensurate effect on the geoid in dynamic models of ascending mantle plumes.

Verification of the pseudo-free-surface algorithm

In order to verify the validity of our pseudo-free-surface algorithm, we have developed analytic solutions for surface relaxation of Stokes' flows using a Green's function method (Parsons & Daly 1983; Solomon, Comer & Head 1982) (Appendix A). The buoyancy-driven flow is confined in a 2-D 1×1 Cartesian box with reflecting boundary conditions on the two side walls and free-surface conditions on the top and bottom boundaries. The non-dimensional buoyancy force is $T(x, z, t) = \cos(kx)\delta(z - z')$, where $k = 2\pi/\lambda$. The buoyancy force is assumed not to vary with time, i.e. only the momentum equation (1) and continuity equation (2) are solved. Both the top and bottom boundaries have zero topography at $t = 0$. The analytic solutions that fully describe the growth of topography on the top and bottom boundaries consist of a summation of two exponential functions of time. The analytic solutions show that the steady-state topography is identical to that from free-slip boundary conditions (Appendix A).

We find that numerical results from our pseudo-free-surface algorithm agree well with the analytic solutions, with relative errors of less than 1 per cent (Fig. 2). Fig. 2(a) shows the time evolution of maximum topography (at $x = 0$) on the top boundary for a case with $\lambda = 1$ and $z' = 0.5$ for both analytic and numerical solutions. The numerical solutions are insensitive to the time increment as long as the time increment is much smaller than the characteristic time for topographic growth (Fig. 2a for two different time increments). For this case, since the buoyancy is located at mid-depth, the time evolution of topography is the same for both the top and bottom boundaries. Fig. 2(b) presents the evolution of maximum topography (at $x = 0$) for the top and bottom boundaries for a case with $\lambda = 2$ and $z' = 0.75$. For this case, the topography on the bottom boundary has a different time dependence from that on the top boundary, and the numerical solution correctly reproduces this behaviour (Fig. 2b). For both cases, 80×80 bilinear elements are used (this mesh is also used for all the following viscous flow models in a 1×1 box). The comparisons between numerical and analytic solutions suggest that our pseudo-free-surface algorithm is accurate as long as the magnitude of topography is significantly smaller than the wavelength of topography and the time increment is sufficiently smaller than the characteristic times for topographic growth.

Relaxation times for various wavelengths and rheological structures

We have studied surface relaxation as a function of wavelength and rheological structure using both viscous and viscoelastic models. The viscous models are identical to the models used earlier for verifying our pseudo-free-surface algorithm except that the bottom boundary is assumed to be free-slip and that the top 60 km layer representing the lithosphere may have a viscosity different from the 10^{21} Pa s background viscosity. A delta-function buoyancy force is located at a depth of 400 km and does not vary with time. The relaxation times do not depend on the depth of the buoyancy force (see Appendix A). The 80×80 mesh is refined within the lithosphere and sufficiently small time increments are used to ensure that the time evolution of topography is resolved. Other model parameters are presented in Table 1.

The time evolution of topography on the top boundary behaves like an exponential function of time (Fig. 3a for a wavelength of 750 km), similar to that with free-surface boundary conditions on both the top and bottom boundaries (Fig. 2a). The steady-state topography for different lithospheric viscosities (Fig. 3a) is identical to that from free-slip boundary models. The models show that the relaxation times are longer for larger lithospheric viscosities and shorter-wavelength topography [in Fig. 3b, the relaxation time is the time when the topography reaches about 61 per cent $(1 - 1/e)$ of the final topography]. For a wavelength of 750 km, an increase in the lithospheric viscosity from 10^{21} to 10^{23} Pa s does not increase

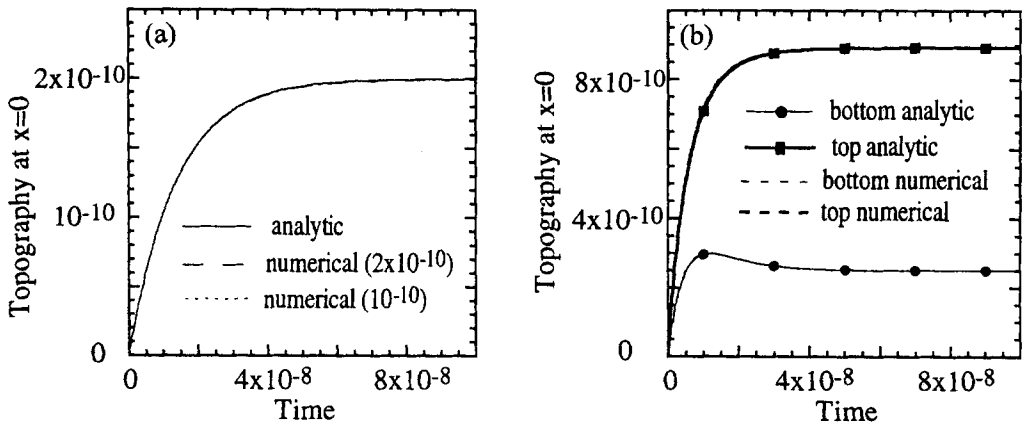

Figure 2. Comparison of time evolution of free surfaces from numerical solutions with that from analytic solutions for a buoyancy-driven flow with a constant viscosity. (a) $z' = 0.5$, $k = 2\pi$; (b) $z' = 0.75$, $k = \pi$.

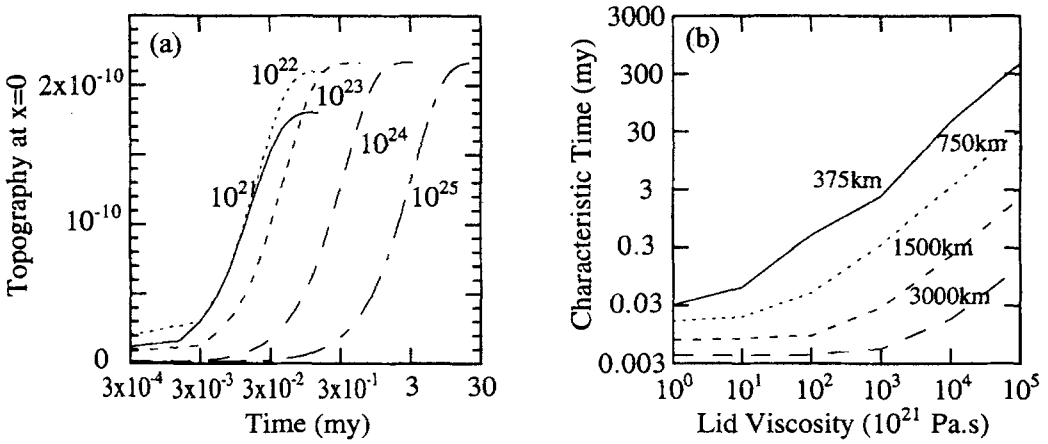

Figure 3. (a) Time evolution of the top surface of a wavelength of 750 km for viscous-flow models with different viscosities in the top 60 km lid. (b) Dependence of characteristic times on the viscosity in the lid for different wavelengths.

the relaxation time significantly (Fig. 3a). However, for viscosities greater than a transitional lithospheric viscosity of 10^{23} Pa s, the relaxation time increases almost linearly as the logarithm of lithospheric viscosity (Fig. 3b). For this wavelength topography and a lithospheric viscosity of 10^{24} Pa s, about 10^6 yr is required for the topography to reach a steady state (Fig. 3a). The transitional lithospheric viscosity is larger for a longer wavelength and is 10^{24} Pa s for a wavelength of 3000 km (Fig. 3b).

We also study surface relaxation in viscoelastic models using TECTON. In the viscoelastic models, only the top boundary is a free surface; all other boundaries are free-slip. Unlike in the viscous models, the motion in the viscoelastic models is driven by surface loads and the coordinates of the top boundary are initially $z(x, 0) = D + d\cos(kx)$, where D is the thickness of box (i.e. 3000 km); d is the maximum perturbation of topography and is 1 km; and $k = 2\pi/\lambda$. The thickness of the lithosphere is assumed to be 90 km. Other model parameters are in Table 1.

In the viscoelastic models, the relaxation times for long wavelengths are not very sensitive to the lithospheric viscosity. The time evolution of the maximum topography at $x = 0$ for a 2000 km wavelength is almost identical for 10^{25} and 10^{27} Pa s viscosity and is only slightly different when the lithosphere has the same viscosity as the background (Fig. 4a). In Fig. 4(a), the initial elastic deformation is about 100 m and depends only on elastic parameters and the initial perturbation in the topography. The relaxation times for shorter wavelengths strongly depend on the lithospheric viscosity. For a 1000 km wavelength, the times required to relax 80 per cent of the initial topography for 10^{23} Pa s and 10^{24} Pa s lithosphere are about 10^5 and 10^6 yr, respectively (Fig. 4b). We also observe that for a 1000 km wavelength the times taken to relax the first 50 per cent of the initial topography are only slightly different for cases with different lithospheric viscosities, but the relaxation becomes much slower for the remaining topography for a higher lithospheric viscosity (Fig. 4b).

The surface relaxation in viscous-flow models is very different from that in viscoelastic models for long-wavelength topography. While the viscous-flow models suggest that for any wavelength there is always a transitional lithospheric viscosity above which the relaxation time increases almost linearly as the logarithm of the lithospheric viscosity (Fig. 3b), the viscoelastic models show that the relaxation time for long wavelengths does not increase significantly with lithospheric viscosity (Fig. 4a), and the relaxation time at long wavelengths is about 10^4 yr, much smaller than the timescale of mantle convection. For wavelengths less than 1000 km, however, both viscous-flow and

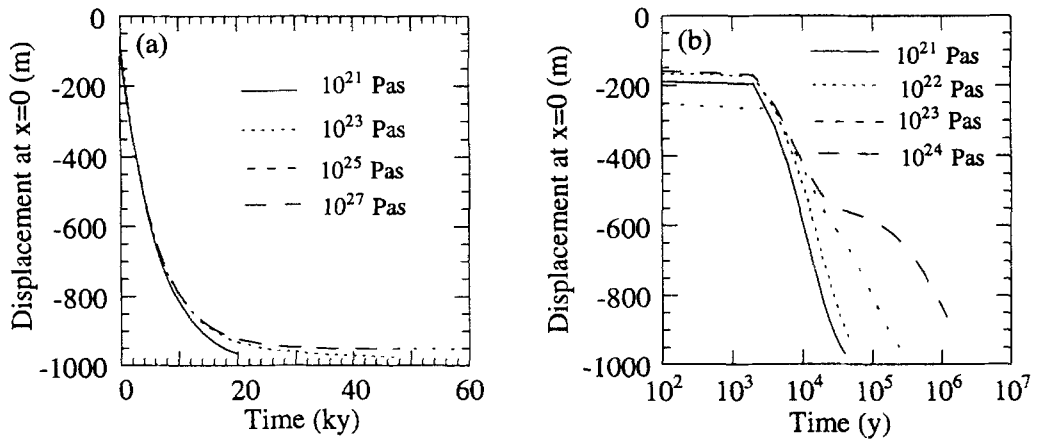

Figure 4. Time evolution of the top surface from viscoelastic models with different viscosities in the top 90 km lid for a wavelength of (a) 2000 km, and (b) 1000 km.

viscoelastic models suggest a strong dependence of relaxation time on lithospheric viscosity (Figs 3a and 4b). For 10^{24} Pa s lithospheric viscosity, the relaxation times can be as large as 10^6 yr, comparable to the timescale of mantle convection.

In models of mantle convection, the large relaxation times for intermediate and short wavelengths (1000 km or less) are significant for calculations of dynamic topography. This suggests that, if the lithospheric viscosity is about 10^{24} Pa s or higher, the topography at intermediate and short wavelengths may be history-dependent, and the topography needs to be determined by directly tracking the evolution of the top boundary with natural free-surface boundary conditions. However, the importance of topographic relaxation can only be determined in time-dependent mantle-convection models in which buoyancy dynamically evolves with time.

Topography over ascending mantle plumes

The influence of surface relaxation on the topography over an ascending plume in a convection model having a free-surface top boundary will be compared with that of models having a free-slip top. In the current set of models, the energy equation is solved, i.e. the buoyancy force dynamically evolves with time.

The plume models are in a 3000 km × 3000 km Cartesian box with 80 × 80 elements. The top 90 km layer represents a high-viscosity lithosphere. The viscosities of the upper and lower mantle are 3.3×10^{20} Pa s and 10^{22} Pa s, respectively. The initial temperature is given as follows: the temperature in the lithosphere increases linearly from 0 °C on the surface to 2000 °C at the bottom of the lithosphere and there is no horizontal temperature gradient within the lithosphere; a plume with 3200 °C temperature, a height of 1000 km, and a width of 60 km is assumed within the lower mantle centred on the left sidewall of the box; the temperature otherwise is uniform and equal to 2000 °C. Since the plume is driven by its own buoyancy in our models, we have assumed that the plume is 1200 °C hotter than the ambient temperature in order to obtain a vertical velocity of approximately 5 cm yr^{-1}. Other model parameters are given in Table 1. For the free-surface calculations, an initial topography on the top boundary (i.e. the free surface) is necessary. We derive this initial topography from a free-slip calculation with the initial buoyancy force; at subsequent time steps, the topography on the top boundary is updated according to our pseudo-free-surface algorithm. The vertical resolution within the lithosphere and the horizontal resolution in the plume are better than 15 km. The horizontal resolution in the vicinity of the plume is also about 15 km. The non-dimensional time increments are 5×10^{-9} (i.e. about 1500 yr in dimensional time) and 2×10^{-8} (about 6000 yr) for cases with free-surface boundary conditions and free-slip boundary conditions, respectively. We have found through resolution studies that these time increments are sufficient to resolve the time-dependent characteristics.

We have computed models with three different lithospheric viscosities: 10^{23} Pa s, 10^{24} Pa s, and 10^{25} Pa s. When the plume rises and approaches the bottom of the lithosphere, the surface topography over the plume grows and the wavelength of the topography decreases (Figs 5, 6a and 6b), in a way which is qualitatively similar to laboratory experiments (Griffiths, Gurnis & Eitelberg 1989). After the plume reaches, and spreads out under, the base of the lithosphere, the magnitude of the topography decreases but the wavelength of the topography increases (Figs 5, 6d and 6e). The rapid growth in the topography at $t = 35$ Myr is due to the increased plume velocity when the plume reaches the relatively low-viscosity upper mantle (Fig. 5). For these three different lithospheric viscosities, calculations with either free-slip or free-surface boundary conditions yield a similar surface topography when the plumes are within the

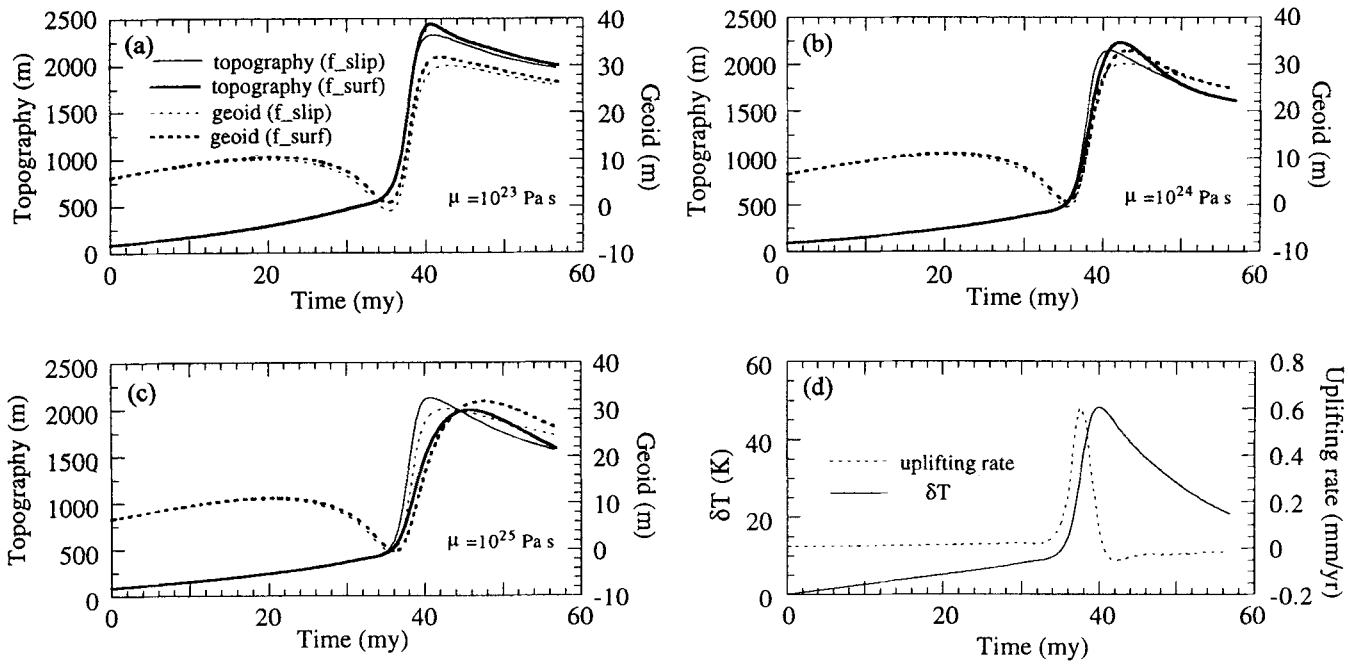

Figure 5. Time histories of topography (solid lines) and geoid (dashed lines) at $x = 0$ for free-slip (thin lines) and free-surface (thick lines) models with a lithospheric viscosity of (a) 10^{23} Pa s, (b) 10^{24} Pa s, and (c) 10^{25} Pa s. (d) Time history of δT ($T_{\text{free-surface}} - T_{\text{free-slip}}$ at $x = 0$ and a depth of 35 km) and rate of surface uplift for 10^{23} Pa s lithosphere.

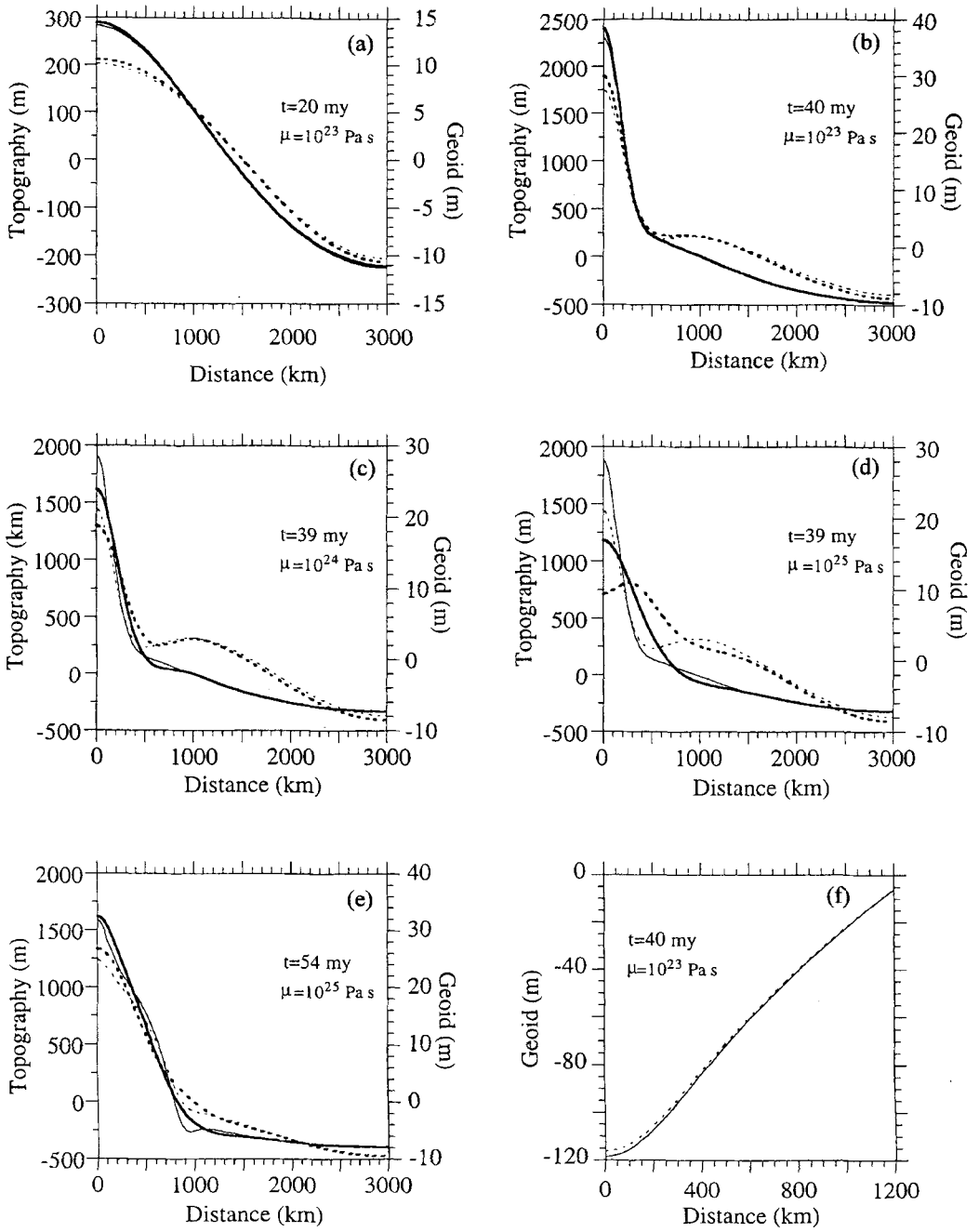

Figure 6. Topography and geoid profiles at (a) $t = 20$ Myr and (b) $t = 40$ Myr for a lithospheric viscosity of 10^{23} Pa s, (c) $t = 39$ Myr for a lithospheric viscosity of 10^{24} Pa s, (d) $t = 39$ Myr and (e) $t = 54$ Myr for a lithospheric viscosity of 10^{25} Pa s. (f) Buoyancy-induced geoid for thermal structure at $t = 40$ Myr for a lithospheric viscosity of 10^{23} Pa s. In (a)–(e), the line convention is the same as that in Fig. 5; in (f) the solid and dashed lines are for free-surface and free-slip calculations, respectively.

lower mantle. When the plumes approach the surface, however, the topographies from free-slip and free-surface calculations become different.

For the case with a lithospheric viscosity of 10^{23} Pa s, when the plume is in the lower mantle, the topography and geoid from the free-surface calculation are almost identical to those from a free-slip calculation (Fig. 6a). The maximum difference in topography at $x = 0$ between the free-surface and the free-slip calculations occurs at $t = 40$ Myr when the plume reaches the bottom of the lithosphere (Figs 7a and b for the thermal structure), with the topography from the free-surface calculation being about 4 per cent larger (Figs 5a and 6b). The topography at $x = 0$ for both the free-slip and the free-surface calculations reaches a maximum at $t = 40$ Myr (Fig. 5a). When the difference in topography reaches a maximum, the geoid at $x = 0$ from the free-surface calculation is about 6 per cent larger than that from the free-slip calculation (Figs 5a and 6b).

When the lithospheric viscosity is 10^{24} Pa s, the magnitude of the maximum topography at $x = 0$ decreases by about 230 m for both methods, when compared with a 10^{23} Pa s lithosphere (Figs 5a and b). Importantly, the topography from the free-surface calculation reaches a maximum about 2 Myr later than

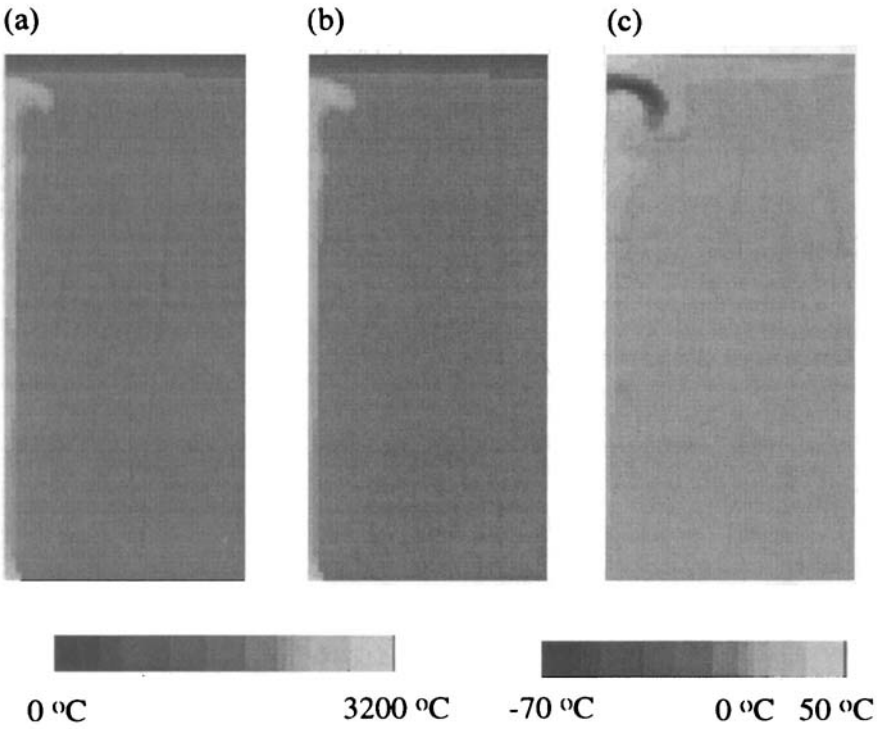

Figure 7. Thermal structure for plumes from (a) free-slip and (b) free-surface calculations at $t = 40$ Myr for a lithospheric viscosity of 10^{23} Pa s; (c) the differential temperature between (a) and (b).

that from the free-slip calculation. Although the maximum topography from the free-surface calculation is larger than that from the free-slip calculation, the topography from the free-slip calculation is larger (Fig. 5b) in the early stages of rapid topographic growth (from 35 to 41 Myr). This difference can be as large as 20 per cent at $t = 39$ Myr (Fig. 6c), and this results in a significant geoid difference (Fig. 6c). The topographies from the free-slip and free-surface calculations converge after 50 Myr.

An increase from 10^{24} to 10^{25} Pa s in lithospheric viscosity does not influence the topography and geoid strongly for free-slip calculations (Figs 5b and c), but causes significant changes for the free-surface calculation (Figs 5b and c). The maximum topography at $x = 0$ is about 150 m less than that from the free-slip calculation (Fig. 5c). The topography reaches a maximum 5 Myr later than that from the free-slip calculation (Fig. 5c). The topography at $x = 0$ from the free-slip calculation is about 60 per cent larger than that from the free-surface calculation at $t = 39$ Myr, and, as a result, causes a local geoid low over the centre of the plume in the free-surface calculation (Figs 5c and 6d). Not surprisingly, the difference in topography and geoid between the free-slip and free-surface calculations diminishes as the plume spreads under the lithosphere (Fig. 6e).

The influence of surface relaxation on topography is greater for shorter wavelengths and larger lithospheric viscosities (Figs 3b, 4a and 4b). When the plumes are in the lower mantle, the surface topography is predominantly long wavelength (Figs 6a and 8a), on which the surface relaxation has a minimal influence (Fig. 6a). As plumes approach the surface, there are increasingly stronger short-wavelength components in the surface topography (Figs 6b, 6c, 6d, 8b and 8c). Surface relaxation retards the development of these short-wavelength components and this influence increases with lithospheric viscosity. As a result, the topography from the free-surface calculation is smoother, with relatively lower power at short wavelengths, and the overall topography from the free-surface calculation grows at a slower rate than with the free-slip calculation (Figs 5b, 5c, 8b and 8c). The critical wavelengths at which the power of the topography from the free-slip case becomes significantly (more than 10 per cent) larger than that from the free-surface case are about 1000 km (i.e. wavenumber 6) and 1500 km (i.e. wavenumber 4) for 10^{24} Pa s and 10^{25} Pa s lithospheric viscosity, respectively (Figs 8b and c). For a large lithospheric viscosity (10^{25} Pa s), the retardation due to surface relaxation can result in a smaller magnitude of maximum topography, compared with that from a free-slip calculation (Fig. 5c). When the plumes spread under the lithosphere, the predominant wavelength in topography increases (Figs 6e and 8d) and the influence of surface relaxation is reduced. As a result, the topographies from free-surface and free-slip calculations converge (Figs 6e and 8d).

Because surface relaxation changes the applied boundary normal stress, it also influences the temperature field. This can be demonstrated with the thermal structure for the case with a 10^{23} Pa s lithospheric viscosity (Fig. 7). The differential temperature between the free-slip (Fig. 7a) and free-surface (Fig. 7b) calculations at $t = 40$ Myr shows that the plume and the overlying lithosphere in the free-surface case are generally about 30 to 45 K hotter (Fig. 7c). There is a narrow layer at the plume head in which the temperature in the free-surface case is about 70 K colder than that in the free-slip case (Fig. 7c). This is because the temperature variation from the plume to lithosphere in the free-surface case is smoother than that in the free-slip case. The differential temperature between the free-surface and free-slip calculations within the lithosphere increases rapidly when the surface uplifts at a relatively fast

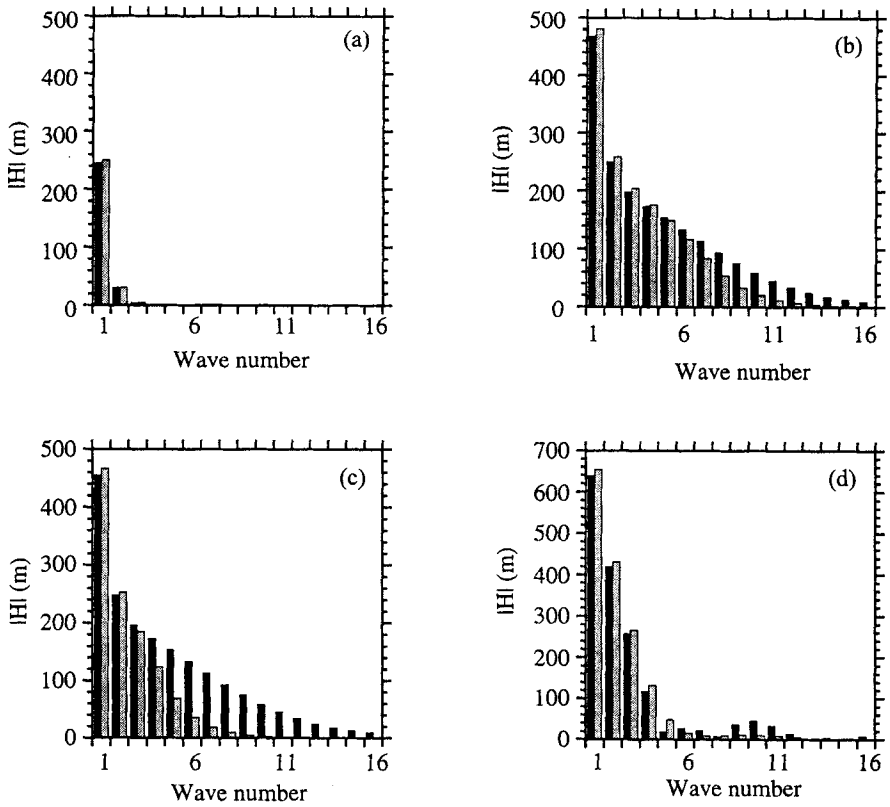

Figure 8. The spectra of topography profiles for free-surface (grey) and free-slip (black) calculations. (a), (b), (c), and (d) are for the profiles in Figs 6(a), (c), (d), and (e), respectively.

rate (Fig. 5d shows the time history of the differential temperature at a depth of 35 km). While the surface is always fixed in free-slip calculations, in the free-surface case the surface uplifts at a maximum rate of about 0.5 mm yr^{-1} (Figs 5a and d). This surface uplifting enhances the plume's vertical motion and results in a hotter lithosphere and mantle in the free-surface case. Since the rate of uplift decreases with lithospheric viscosity (Figs 5a, b, and c), the differential temperature is smaller for a higher-viscosity lithosphere. For a lithospheric viscosity of 10^{25} Pa s at $t = 39$ Myr (Fig. 5c), the lithosphere is about 25 K hotter than that in the free-slip calculation. The generally hotter mantle and lithosphere in the free-surface case (Fig. 5d) cause the topography (4 per cent) and buoyancy-induced geoid (3 per cent) to have larger magnitudes than in the free-slip calculation (Figs 5a, 6b and 6f).

DISCUSSION

The Earth's surface is a natural stress-free boundary. The introduction of a stress-free top boundary in a model of the mantle may influence the dynamics in two ways, compared with models assuming a free-slip boundary. First, the topography on the free-surface boundary is explicitly history-dependent, and this history dependence may be very important in influencing the intermediate- and short-wavelength (1000 km or less) topography for large lithospheric viscosities (Figs 6c and d). Second, by allowing vertical motion on the surface, the free surface enhances the vertical flow in the mantle interior and this influences the mantle temperature field, especially in the shallow part of the mantle (e.g. Figs 7c and 5d). The influence of a free surface on the shallow mantle thermal structure is larger when the free surface experiences a greater vertical motion (Figs 5d and 7c). The hotter lithospheric thermal structure over mantle plumes from the free-surface calculation may have important implications in studying the detailed thermal structure and melting problems in spreading centres and magma chambers—these problems have been traditionally studied with free-slip or fixed-velocity boundary conditions (e.g. Chen & Morgan 1990).

When the timescale of topographic growth is comparable to the timescale for moving mantle buoyancy, the history dependence of topography must be included in mantle dynamical models by using a free-surface formulation. If the lithosphere has an effective viscosity of 10^{24} Pa s or higher, the topographic growth time for a wavelength of 1000 km can be as large as 1 Myr, for both viscous and viscoelastic models (Figs 3 and 4b). The surface relaxation retards the topographic growth at relatively short wavelengths (about 1000 km or less) and thus smoothes the topography (Figs 6 and 8). The surface relaxation has a major influence on topographic growth over ascending plumes (Fig. 5) and in back-arc basins over subducting slabs (Part II).

For a wavelength longer than 2000 km, the relaxation times from viscous-flow models can still be as large as 1 Myr (Fig. 3b), but the relaxation times from viscoelastic models seem to be always less than 10^5 yr, independent of the lithospheric viscosity (Fig. 4a), indicating that for long wavelengths the relaxation time is controlled by the viscoelastic properties of the lithosphere. This suggests that caution should be exercised in interpreting surface relaxation results from viscous models for wavelengths longer than 2000 km. For our viscous-flow

models of mantle plumes with lithospheric viscosities of 10^{24} and 10^{25} Pa s, the wavelength at which the topography is significantly influenced by surface relaxation is about 1000 km (Figs 8c and d). Therefore, we believe that our results will not be significantly influenced by more realistic viscoelastic constitutive relations. To formulate viscoelastic models for large deformations such as that caused by mantle convection is difficult (e.g. Harder 1991).

Our free-surface algorithm works for surfaces with topographies having a small ratio of amplitude to wavelength. The time increment for this algorithm must be sufficiently small, in order to ensure stability. We do not attempt to give a stability criterion for this algorithm, because the stability criterion may depend on factors such as lithospheric viscosity and the wavelength of topography. For a single-harmonic topography, in order to resolve the time evolution of the topography the time increment should be smaller than the relaxation time, which depends on the lithospheric viscosity. For a topography with many different wavelengths, the time increment presumably is limited by the smallest relaxation time, which is commonly associated with the longest-wavelength component of the topography. In practice, we perform resolution studies to guarantee the convergence and stability of our solutions. This algorithm is easy to implement and can be applied to other numerical methods such as finite-difference and finite-volume methods.

CONCLUSIONS

For short and intermediate wavelengths (1000 km or less) and/or a high lithospheric viscosity ($> 10^{24}$ Pa s), both viscoelastic and viscous models suggest that the characteristic time for developing surface topography is comparable to the time-scale of mantle convection (10^6 yr). Under these conditions, dynamic topography is history-dependent and the surface relaxation has to be included in mantle dynamic models by using a natural stress-free boundary. We have developed a new Eulerian finite-element technique to model free surfaces; this enables us to study long-term dynamics of free surfaces in the presence of evolving buoyancy. By comparing numerical with analytic solutions of viscous relaxation for fixed-buoyancy problems, we find that our method is very accurate, with relative errors of less than 1 per cent, as long as the magnitude of the topography is much smaller than the wavelength. In applying this technique to dynamic models of mantle plumes, we find that surface relaxation retards the growth of short- and intermediate-wavelength (1000 km or less) topography and yields a smoother topography for a lithospheric viscosity of 10^{24} to 10^{25} Pa s. This has a significant influence on the geoid at the corresponding wavelengths. By allowing vertical motion on the free surface, models with a free-surface boundary yield a hotter lithosphere over an ascending plume, compared with the thermal structure from the free-slip formulation.

ACKNOWLEDGMENTS

We wish to thank D. Kemp and C. Eloy for helpful discussions, and H. J. Melosh of the University of Arizona for providing the TECTON code. This work was supported by the David and Lucile Packard Foundation and NSF grants EAR-9496185 and EAR-9417645. SZ was partly supported by a Texaco Fellowship at Caltech. This is contribution 5616 of the Division of Geological and Planetary Sciences, California Institute of Technology.

REFERENCES

Anderson, D.L., 1995. Lithosphere, asthenosphere, and perisphere, *Rev. Geophys.*, **33,** 125–149.

Braun, J. & Sambridge, M., 1995. A numerical method for solving partial differential equations on highly irregular evolving grids, *Nature,* **376,** 655–660.

Cathles, L.M., 1975. *The Viscosity of the Earth's Mantle,* Princeton University Press, Princeton, NJ.

Chen, Y. & Morgan, W.J., 1990. A nonlinear rheology model for midocean ridge axis topography, *J. geophys. Res.,* **95,** 17 583–17 604.

Davies, G.F., 1988. Role of the lithosphere in mantle convection, *J. geophys. Res.,* **93,** 10 451–10 466.

Griffiths, R.W., Gurnis, M. & Eitelberg, G., 1989. Holographic measurements of surface topography in laboratory models of mantle hotspots, *Geophys. J.,* **96,** 477–495.

Gurnis, M., Eloy, C. & Zhong, S., 1995. Free-surface formulation of mantle convection—II. Implications to subduction zone observables, *Geophys. J. Int.,* **127,** 719–727 (this issue).

Hager, B.H., 1984. Subducted slabs and the geoid: constraints on mantle rheology and flow, *J. geophys. Res.,* **89,** 6003–6015, 1984.

Harder, H., 1991. Numerical simulation of thermal convection with Maxwellian viscoelasticity, *J. Non-Newt. Fluid Mech.,* **39,** 67–88.

Haskell, N.A., 1935. The motion of a viscous fluid under a surface load, *Physics,* **6,** 265–269.

Hughes, T.J.R., Liu, W.K. & Zimmermann, T.K., 1981. Lagrangian–Eulerian finite element formulation for incompressible viscous flows, *Comput, Meths. appl. Mech. Engrg,* **29,** 329–349.

Karato, S. & Wu, P., 1993. Rheology of the upper mantle: a synthesis, *Science,* **260,** 771–778.

King, S.D., Raefsky, A. & Hager, B.H., 1990. ConMan: vectorizing a finite element code for incompressible two-dimensional convection in the Earth's mantle, *Phys. Earth planet. Inter.,* **59,** 195–207.

McConnell, R.K., Jr, 1968. Viscosity of the mantle from relaxation time spectra of isostatic adjustment, *J. geophys. Res.,* **73,** 7089–7105.

Melosh, H.J. & Raefsky, A., 1980. The dynamical origin of subduction zone topography, *Geophys. J. R. astr. Soc.,* **60,** 333–354.

Parsons, B. & Daly, S., 1983. The relationship between surface topography, gravity anomalies and the temperature structure of convection, *J. geophys. Res.,* **88,** 1129–1144.

Poliakov, A.N.B. & Podladchikov, Yu.Yu., 1992. Diapirism and topography, *Geophys. J. Int.,* **109,** 553–564.

Ricard, Y., Fleitout, L. & Froidevaux, C., 1984. Geoid heights and lithospheric stresses for a dynamical Earth, *Ann. Geophys.,* **2,** 267–286.

Richards, M.A. & Hager, B.H., 1984. Geoid anomalies in a dynamic Earth, *J. geophys. Res.,* **89,** 5987–6002.

Richards, M.A., Hager, B.H. & Sleep, N.H., 1988. Dynamically supported geoid highs over hotspots: observation and theory, *J. geophys. Res.,* **93,** 7690–7708.

Solomon, S.C., Comer, R.P. & Head, J.W., 1982. The evolution of impact basins: viscous relaxation of topographic relief, *J. geophys. Res.,* **87,** 3975–3992.

Watts, A.B., Bodine, J.H. & Ribe, N.M., 1980. Observations of flexure and the geological evolution of the Pacific Ocean basin, *Nature,* **283,** 532–537.

Zhong, S. & Gurnis, M., 1994. Controls on trench topography from dynamic models of subducted slabs, *J. geophys. Res.,* **99,** 15 683–15 695.

APPENDIX A: ANALYTIC SOLUTIONS FOR VISCOUS RELAXATION OF BUOYANCY-INDUCED TOPOGRAPHY

We combine the solution strategy used by Solomon *et al.* (1982) for the relaxation of surface loads with a Green's function method (Parsons & Daly 1983) to derive the analytic solutions

for viscous relaxation for buoyancy-induced topography in a 2-D Cartesian box for an isoviscous fluid. For this surface relaxation problem, both the top and bottom boundaries are assumed to be stress-free and have no topography at $t=0$. A buoyancy force $\cos(kx)\delta(z-z')$ is placed at $z=z'$ when $t=0$, and the buoyancy does not evolve with time. We seek an analytic solution which describes the time evolution of topography on both the top and bottom free surfaces.

The momentum equation coupled with an incompressibility equation for buoyancy $\cos(kx)\delta(z-z')$ can be expressed in terms of a stream function as

$$\frac{\partial^4\phi}{\partial x^4}+2\frac{\partial^4\phi}{\partial x^2\partial z^2}+\frac{\partial^4\phi}{\partial z^4}=\cos(kx)\delta(z-z'). \tag{A1}$$

Solutions for arbitrary buoyancy can be expressed in an integral form of the solution ϕ of (A1) (e.g. Parsons & Daly 1983). The general solution of (A1) is

$$\phi=k\sin(kx)[A_1\sinh(kz)+B_1\cosh(kz)+C_1z\sinh(kz)+D_1z\cosh(kz)],\quad \text{for } z<z'; \tag{A2}$$

$$\phi=k\sin(kx)[A_2\sinh(k\tilde{z})+B_2\cosh(k\tilde{z})+C_2\tilde{z}\sinh(k\tilde{z})+D_2\tilde{z}\cosh(k\tilde{z})],\quad \text{for } z>z'; \tag{A3}$$

where $\tilde{z}=z-1$; A_1, B_1, C_1, D_1, A_2, B_2, C_2 and D_2 are functions of time t and will be determined by boundary conditions and the continuity equations at $z=z'$. We can relate non-dimensional velocity, stress, and pressure to ϕ with

$$u_x=-\frac{\partial\phi}{\partial z},\qquad u_z=\frac{\partial\phi}{\partial x},\qquad \tau_{xz}=\left(\frac{\partial^2\phi}{\partial x^2}-\frac{\partial^2\phi}{\partial z^2}\right), \tag{A4}$$

$$P=Qz+k\cos(kx)\left(\frac{1}{k}\frac{\partial^3\phi}{\partial z^3}-k\frac{\partial\phi}{\partial z}\right),\qquad \sigma_{zz}=-P+2\frac{\partial^2\phi}{\partial x\partial z}. \tag{A5}$$

P is the pressure including the hydrostatic pressure; Q is the non-dimensional parameter $\rho g D^3/(\mu\kappa)$; ρ is the density of the fluid; μ is the viscosity; κ is the thermal diffusivity; D is the thickness of the box; and g is the gravity. Assume that the top and bottom boundaries can be represented, respectively, as

$$\xi(x,t)=F(t)\cos(kx),\qquad \zeta(x,t)=G(t)\cos(kx). \tag{A6}$$

On the two free surfaces, the boundary conditions can be written as (e.g. Solomon *et al.* 1982)

$$\tau_{xz}=0,\quad \text{for } z=0 \text{ and } z=1; \tag{A7}$$

$$\sigma_{zz}=0,\quad \text{for } z=\xi; \tag{A8}$$

$$\sigma_{zz}=-Q-Q\frac{\rho_u}{\rho}\zeta,\quad \text{for } z=\zeta; \tag{A9}$$

where ρ_u is the density for the flow underneath the layer. We also have the kinematic equations

$$u_z=\dot{\xi}(x,t)=\dot{F}(t)\cos(kx),\quad \text{for } z=0; \tag{A10}$$

$$u_z=\dot{\zeta}(x,t)=\dot{G}(t)\cos(kx),\quad \text{for } z=1. \tag{A11}$$

The continuity equations at $z=z'$ (Parsons & Daly 1983) are

$$\phi|_{z=z'+}=\phi|_{z=z'-};\qquad \left.\frac{\partial\phi}{\partial z}\right|_{z=z'+}=\left.\frac{\partial\phi}{\partial z}\right|_{z=z'-}; \tag{A12}$$

$$\left.\frac{\partial^2\phi}{\partial z^2}\right|_{z=z'+}-\left.\frac{\partial^2\phi}{\partial z^2}\right|_{z=z'-}=\cos(kx); \tag{A13}$$

Substituting (A2) to (A6) into the 10 equations from (A7) to (A13) and eliminating the eight parameters of (A2) and (A3), we can obtain two coupled equations for solving $F(t)$ and $G(t)$:

$$F\frac{Q}{2k}=\frac{[\sinh(k)+k\cosh(k)]\dot{G}-[k+\sinh(k)\cosh(k)]\dot{F}}{\sinh^2(k)}+M, \tag{A14}$$

$$G\frac{Q\Delta\rho}{2k\rho}=\frac{[k+\sinh(k)\cosh(k)]\dot{G}-[k\cosh(k)+\sinh(k)]\dot{F}}{\sinh^2(k)}+N, \tag{A15}$$

where

$$M=\frac{kz'\sinh(k)\cosh(kz'-k)-k\sinh(kz')-\sinh(k)\sinh(kz'-k)}{2k\sinh^2(k)}, \tag{A16}$$

$$N=\frac{kz'\sinh(k)\cosh(kz')-k\cosh(k)\sinh(kz')-\sinh(k)\sinh(kz')}{2k\sinh^2(k)}, \tag{A17}$$

and $\Delta\rho=\rho-\rho_u$. From (A14) to (A17), it is clear that when both the top and bottom topographies reach steady state (i.e., $\dot{F}=\dot{G}=0$), they are identical to the topography with free-slip boundary conditions (e.g. Parsons & Daly 1983). (A14) and (A15) can be solved with an eigenvector method. The solution is

$$F(t)=\frac{\beta\gamma m_1[\exp(l_1t)-1]}{(\lambda_1-\alpha)l_1}+\frac{\beta\gamma m_2[\exp(l_2t)-1]}{(\lambda_2-\alpha)l_2}, \tag{A18}$$

$$G(t)=\frac{m_1[\exp(l_1t)-1]}{l_1}+\frac{m_2[\exp(l_2t)-1]}{l_2}, \tag{A19}$$

where

$$\alpha=Q\frac{k+\cosh(k)\sinh(k)}{2k[k^2-\sinh^2(k)]},$$

$$\beta=Q\frac{k\cosh(k)+\sinh(k)}{2k[k^2-\sinh^2(k)]},\qquad \gamma=\frac{\Delta\rho}{\rho}, \tag{A20}$$

$$\lambda_{1,2}=\frac{\alpha(1+\gamma)\pm\sqrt{(1+\gamma)^2\alpha^2-4\gamma(\alpha^2-\beta^2)}}{2}, \tag{A21}$$

$$l_1=\frac{\lambda_2\lambda_1-\alpha(1+\gamma)\lambda_1+(\alpha^2-\beta^2)\gamma}{\lambda_2-\lambda_1},$$

$$l_2=\frac{\alpha(1+\gamma)\lambda_2-\lambda_2\lambda_1-(\alpha^2-\beta^2)\gamma}{\lambda_2-\lambda_1}, \tag{A22}$$

$$X=\frac{2k(\beta N-\alpha M)}{Q},\qquad Y=\frac{2k(\alpha N-\beta M)}{Q}, \tag{A23}$$

$$m_1=\frac{(\alpha-\lambda_1)[(\alpha-\lambda_2)X+\beta\gamma Y]}{(\lambda_2-\lambda_1)\beta\gamma},$$

$$m_2=\frac{(\alpha-\lambda_2)[-(\alpha-\lambda_1)X-\beta\gamma Y]}{(\lambda_2-\lambda_1)\beta\gamma}. \tag{A24}$$